

# Skyrmion solids in monolayer graphene

H. Zhou,<sup>1</sup> H. Polshyn,<sup>1</sup> T. Taniguchi,<sup>2</sup> K. Watanabe,<sup>2</sup> and A.F. Young<sup>1</sup>

<sup>1</sup>*Department of Physics, University of California, Santa Barbara CA 93106 USA*

<sup>2</sup>*National Institute for Materials Science, Tsukuba, Ibaraki 305-0044, Japan*

(Dated: April 26, 2019)

**Partially filled Landau levels host competing orders, with electron solids prevailing close to integer fillings before giving way to fractional quantum Hall liquids as the Landau level fills[1, 2]. Here, we report the observation of an electron solid with noncolinear spin texture in monolayer graphene, consistent with solidification of skyrmions[3]—topological spin textures characterized by quantized electrical charge[4, 5]. In electrical transport, electron solids reveal themselves through a rapid metal-insulator transition in the bulk electrical conductivity as the temperature is lowered[6], accompanied by the emergence of strongly nonlinear dependence on the applied bias voltage[7, 8]. We probe the spin texture of the solids using a modified Corbino geometry[9, 10] that allows ferromagnetic magnons to be launched and detected[11, 12]. We find that magnon transport is highly efficient when one Landau level is filled ( $\nu = 1$ ), consistent with quantum Hall ferromagnetic spin polarization; however, even minimal doping immediately quenches the the magnon signal while leaving the vanishing low-temperature charge conductivity unchanged. Our results can be understood by the formation of a solid of charged skyrmions near  $\nu = 1$ , whose noncolinear spin texture leads to rapid magnon decay. Data near fractional fillings further shows evidence for several fractional skyrmion crystals, suggesting that graphene hosts a vast and highly tunable landscape of coupled spin and charge orders.**

When a spin-degenerate Landau level is half filled (corresponding to filling factor  $\nu = 2\pi\ell_B^2 n = 1$  with the magnetic length  $\ell_B = (eB_\perp/\hbar)^{-1/2}$  and  $n$  the carrier density), dominant exchange interactions drive the system into an insulating quantum Hall ferromagnetic (QHFM) state[13]. Notably, only minimal anisotropy is introduced by the Zeeman energy ( $E_Z = g\mu_B B_T$ ), which is much smaller than the exchange energy ( $E_X = \sqrt{\frac{\pi}{2}} \frac{e^2}{\epsilon\ell_B}$ ). As a result, smooth skyrmion spin textures, which minimize exchange energy at the expense of reversing more spins relative to the external magnetic field, can be energetically favorable[4]. In contrast to skyrmions in metallic magnets, quantum Hall skyrmions have quantized electrical charge, leading to strong inter-skyrmion interactions and predicted spatial ordering of finite density skyrmions[3]. While thermal measurements[14–16], microwave spectroscopy[17], nuclear magnetic resonance and polarized absorption spectroscopy[18–26] all show signatures of skyrmion solids, many features of these states of matter remain unexplored, including their degree of crystalline order and the nature of their elementary excitations.

Owing to its wide range of electrostatic tunability and ex-

perimental accessibility, graphene provides a potentially ideal platform for probing the phase diagram of skyrmion solids. For example, the exposed surface may allow direct magnetic imaging, and the high sample quality permits the exploration of skyrmion ground states over a broad range of electron density, magnetic field, and single particle wave function structure. However, conventional detection schemes that rely on coupling to nuclear spins are challenging in carbon  $\pi$ -orbitals, and evidence to date for skyrmion physics in graphene has been limited to their indirect impact on measured energy gaps [27–29]. Indeed, while electron solids were recently reported in graphene in higher Landau levels[30], no evidence has been reported for electron solidification of any kind within the lowest Landau level where skyrmion solids are theoretically anticipated.

To explore the phase diagram of electron solids in graphene, we study ultra-high quality monolayer graphene devices fabricated in a Corbino geometry (see Methods). Two patterned graphite local gates and a doped p-Si global gate provide independent control of carrier density in two contact regions (II and III, rendered in pink and green in Fig. 1a), in addition to the bottom gated bulk of region I. The electrical conductance,  $G$ , between two contact ‘islands’ is directly proportional to the bulk electrical conductivity  $\sigma_{xx}$ . Figs. 1b-d show temperature dependent measurements of  $G$  for  $0 < \nu < 1$ . Deep sequences of fractional quantum Hall(FQH) states manifest as conductance minima at fractional  $\nu = \frac{p}{mp \pm 1}$  and  $\nu = 1 - \frac{p}{mp \pm 1}$  with  $m = 2, 4$ , corresponding to the two-flux and four-flux composite fermion sequences. The data also feature anomalous insulating states near  $\nu = 0$  and  $\nu = 1$ , extending beyond the  $\nu = 1/5$  and  $4/5$  FQH states, respectively, which interrupt this insulating behavior. In contrast to even weak FQH states, which show a monotonic, simply activated temperature dependence up to temperatures of several Kelvin, the conductivity of the anomalous insulators transitions from metallic ( $dG/dT < 0$ ) to insulating ( $dG/dT > 0$ ) temperature coefficient at  $T \sim 300 - 600$  mK (Fig. 1d).

The temperature dependence and density range of the anomalous insulators strongly resemble results obtained in clean semiconductor quantum wells[6, 31], attributed to charge solidification at low quasiparticle density. In semiconductors, solidification was shown to be accompanied by the onset of nonlinear transport at anomalously low threshold electric fields, interpreted as depinning of the solid phases[7, 8]. We observe similar behavior in a range of fillings near  $\nu = 1$  (Fig. 1e), and near other integer  $\nu$  in the lowest Landau level (Fig. S1). Whereas the insulating states at integer and fractional fillings are highly robust to applied bias, the

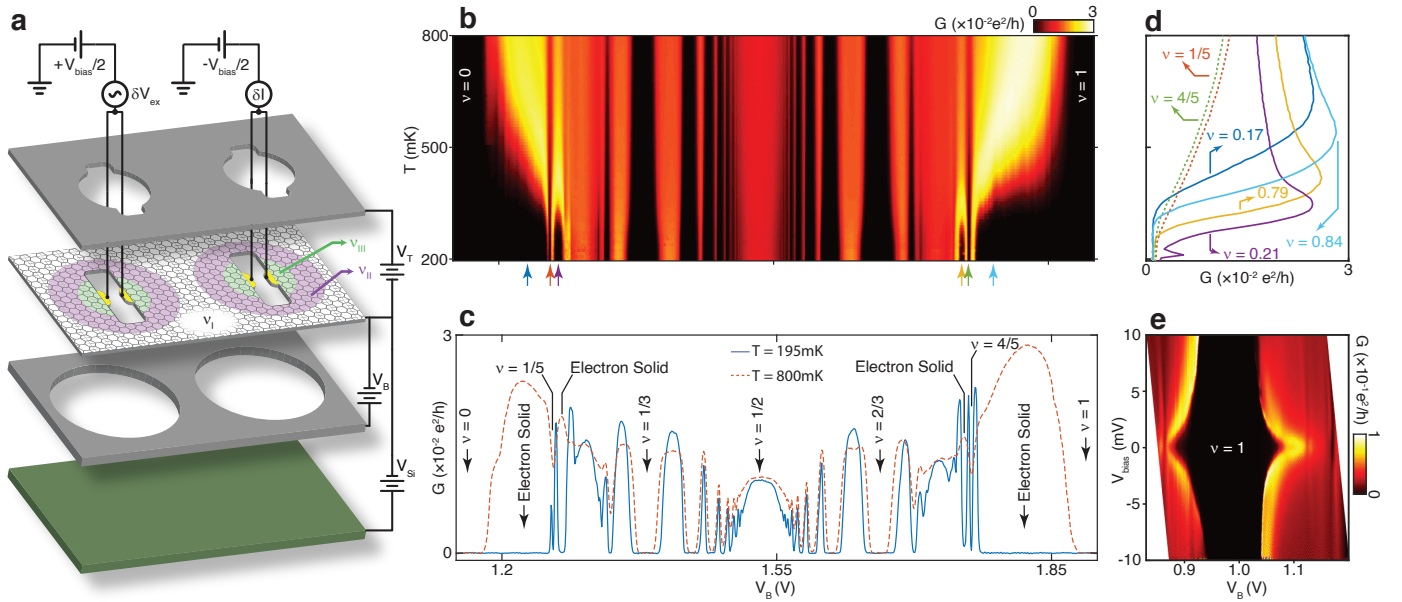


**FIG. 1. Electron solid phases in the lowest Landau level.** **a**, Device and measurement schematic. Voltages applied to graphite top- and bottom-gates ( $V_T$  and  $V_B$ ) and an additional silicon gate ( $V_{Si}$ ) allow independent control of  $\nu$  in regions I (white), II (pink), and III (green). The differential conductance  $G = \delta I / \delta V_{ex}$ , proportional to the bulk conductivity of region I, is measured as shown, with  $\delta V_{ex}$  an applied low frequency voltage excitation and  $\delta I$  the induced current across the  $\nu_I$  region. The DC bias  $V_{bias} = 0$  unless indicated. **b**, Temperature-dependent  $G$  for  $0 < \nu < 1$  at  $B_{\perp} = 13.5T$ . **c**,  $G$  measured at  $T = 195mK$  and  $T = 800mK$ . Labels highlight a subset of the observed insulating states, including FQH and electron solid phases. **e**,  $G$  measured as a function of  $T$  for several values of  $V_B$ , indicated by colored arrows in panel **c**. The hallmark of the electron solid phases is a sign reversal in  $dG/dT$ . **f**,  $G$  near  $\nu = 1$  at  $B_{\perp} = 10T$  measured as a function of  $V_B$  and  $V_{bias}$ .

anomalous insulators near integer  $\nu$  rapidly vanish at low bias voltages  $V_{bias} \sim 1mV$ . Taken together, the temperature and bias dependent transport data show that electron solid phases are a generic feature of the graphene lowest Landau level.

While the electron solids proximal to  $\nu = \pm 2$ ,  $\nu = \pm 1$ , and  $\nu = 0$  show only quantitative differences in their electrical transport properties, they are predicted to arise from solidification of quasiparticles with qualitatively different spin textures. In the case of  $\nu = \pm 2$ , corresponding to a completely empty or full Landau level, one expects solidification of bare electrons or holes. While the electron solid is thought to have a ferromagnetic ground state[32], exchange interactions are weaker than typical experimental temperatures, making the physically realized state paramagnetic. Near charge neutrality, in contrast, the spin texture of the electron solid should depend on the nature of the  $\nu = 0$  ground state, which is thought to be a canted antiferromagnet or charge density wave in graphene samples with sublattice symmetry breaking[33] (see Fig. S2). In the former case, noncolinear spin textures are expected for some range of  $\nu$ , while the latter should be paramagnetic by analogy with  $\nu = \pm 2$ . Finally, at  $\nu = \pm 1$  the low energy charged excitations are spin reversals, whose nature depends on the ratio  $\kappa = E_Z/E_X$ . At large  $\kappa$ , the electron solid polarizes in a single spin branch; however, for sufficiently low  $\kappa$ , the spin-reversed excitations are skyrmions, and the solid should have long wavelength noncolinear spin texture[3].

To probe the spin texture of the electron solids, we measure

the bulk transport of magnons[11, 12], as depicted schematically in Fig. 2a. Magnon transport is measured by setting  $\nu_{III} = 2$  and  $\nu_{II} = 1$ , creating lateral heterojunctions near each pair of contacts, which serve as a magnon launcher and magnon detector, respectively. Applying a voltage bias  $eV_{bias} \geq E_Z$  across contacts in the injector island launches neutral magnons into the electrically insulating  $\nu_{II} = 1$  region. The probability of transporting a magnon across region I is then encoded in the nonlocal response measured across the  $\nu_I$  sample bulk,  $\delta V_{nl} / \delta V_{ex}$ , where  $\delta V_{ex}$  is a small AC voltage applied in series with  $V_{bias}$  across the injector and  $\delta V_{nl}$  is the AC voltage measured across the detector. Note that in this measurement, the relevant magnons are excitations of the  $\nu_{II} = 1$  QHFM, which have quantized spin of one in the direction anti-parallel to the applied magnetic field and energy dispersion  $E(k) = E_Z + \alpha k^2$ [4, 11, 34]. The nonlocal response for  $eV_{bias}$  slightly larger than  $E_Z$  thus measures the probability of transmitting low-k magnons from injector to detector through region I. This signal can be suppressed either by the absence of compatible neutral modes in the intervening region, or by the presence of additional decay channels by which incoming magnons can relax their energy and momentum outside the spin system.

Figs. 2b-c show data taken in this configuration. For all  $\nu_I$ ,  $\delta V_{nl} = 0$  for  $eV_{bias} < E_Z$ , indicating that the measured response indeed arises from magnon transport. No nonlocal responses are observed in the nonmagnetic  $\nu_I = 2$  state or in

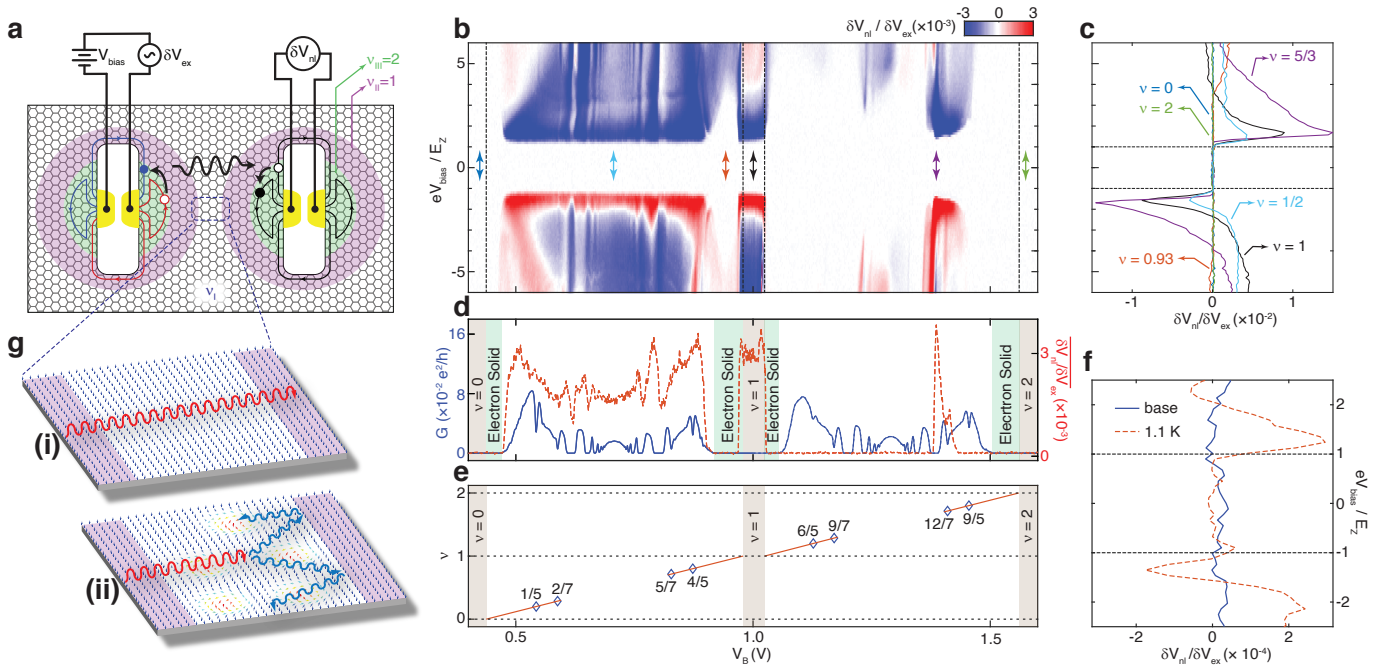


**FIG. 2. Skyrmion solid phase near  $\nu = 1$ .** **a**, Schematic for measuring magnon transport. Nonlocal measurements are performed with  $\nu_{\text{III}} = 2$  and  $\nu_{\text{II}} = 1$ . Applying  $eV_{\text{bias}} > E_Z$  launches magnons through region II, in which magnons can propagate freely. The charge insulating bulk of region II prevents electron flow for all  $\nu$ . Magnons transmitted through region I and back into the detector are absorbed generating the measured nonlocal voltage. **b**, False-color plot of the non-local response for  $0 < \nu_1 < 2$  as function of  $eV_{\text{bias}}/E_Z$  and  $V_B$  at  $B_{\perp} = 10\text{T}$ . **c**, Non-local response as a function of  $eV_{\text{bias}}/E_Z$  for different values of  $V_B$ , corresponding to the colored arrows in panel **a**. The dashed lines mark the Zeeman threshold  $eV_{\text{bias}}/E_Z = \pm 1$ , and approximate  $\nu$  for each curve are indicated. **d**, Blue: Local conductance  $G$  for  $0 < \nu < 2$ . Red: Root-mean-square average of the non-local response in the range  $-1.5E_Z < eV_{\text{bias}} < 1.5E_Z$ . Boundaries between integer quantum Hall gaps and electron solids are indicated by the shaded regions. **e**, The symbols denote  $\nu$  as determined from the positions in  $V_B$  of FQH states associated with  $\nu_1 = 1/5, 2/7, 5/7, 4/5, 6/5, 9/7, 12/7$  and  $9/5$  as function of  $V_B$ . Red lines represent extrapolations of  $\nu$  to the nearest integer determined using pairs of adjacent FQH states. Shaded regions denote the finite extent in  $V_B$  of states with integer  $\nu$ . Nonlocal response at base temperature (blue) and  $T=1.1\text{K}$  (red) near  $\nu = 1$ . Lines represent data averages over a range of  $0.927 < V_B < 0.955\text{V}$ . **g**, Magnon decay in a skyrmion solid. (i) When  $\nu_1 = 1$ , QHFM magnons are transmitted with little loss. (ii) When region I is in a skyrmion solid phase, magnons rapidly decay into other magnetic modes with  $E < E_Z$  and spin less than one. These modes cannot enter the  $\nu_{\text{II}} = 1$  detector region, leading to suppression of the nonlocal response.

the  $\nu = 0$  state. Among the strongest nonlocal responses are observed at  $\nu_1 = 1$  and  $5/3$ . This is consistent with theoretical expectations of a fully spin-polarized QHFM (for  $\nu = 1$ ) and fully spin-polarized fractional QHFM (at  $\nu = 5/3$ ), both of which are predicted to admit long-distance transport of ferromagnetic magnons[35]. The nonlocal response is not correlated with the charge conductivity (Fig. 2d). While the two regions  $0 < \nu < 1$  and  $1 < \nu < 2$  show similar sequences of FQH states, they differ markedly in their nonlocal response, reflecting differing ground state spin structure across the lowest Landau level.

To determine the boundaries of the electron solid in Fig. 2b, we calibrate the electron density using weakly formed FQH states from the four flux sequence (Fig. 2e). This analysis shows an electron solid regime of vanishing low-temperature  $G$  but finite quasiparticle density near each integer  $\nu$ , consistent with the temperature dependent and nonlinear transport measurements described above. Comparison with the nonlocal response shows that all four electron solids suppress magnon transport. Near  $\nu = 2$ , this is consistent with a param-

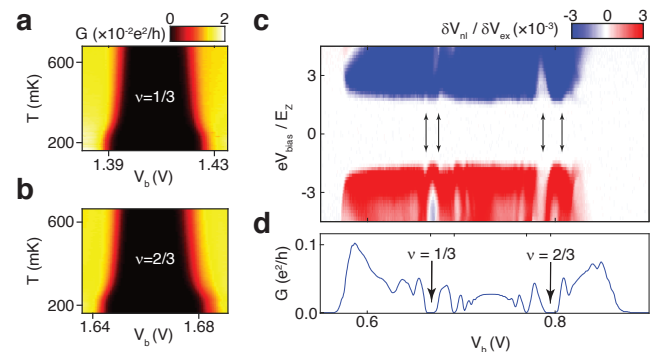


**FIG. 3. Evidence for fractional Skyrmion solid phases.** **a** Temperature-dependent conductance near  $\nu = 1/3$  and **(b)**  $\nu = 2/3$ , showing a low-temperature transition to an insulator at small values of  $|\nu - 1/3|$  and  $|\nu - 2/3|$ . **c**, Non-local voltage for  $0 < \nu < 1$  as a function of  $V_B$  and  $V_{\text{bias}}$  at  $B_{\perp} = 7\text{T}$ . Arrows point indicate regions of suppressed non-local response near the Zeeman threshold, reminiscent of the skyrmion signature observed near  $\nu = 1$ . **d**, Conductance within the same carrier density range as **(a)**.

agnetic electron solid, while at  $\nu = 0$  the solid presumably has noncollinear spin textures or is also a paramagnet. Notably, in both cases the electron solid is not distinguishable from its parent integer state by either its low temperature charge conductivity or its magnon transport, both of which vanish. This is in sharp contrast to the solids surrounding  $\nu = 1$ , which do not allow magnon transport in contrast to their quantum Hall ferromagnetic parent state. Remarkably, the boundary of magnon transport aligns precisely with the edges of the  $\nu = 1$  gap determined from quantum capacitance considerations (see also Fig. S4). We thus conclude that while the QHFM at exactly  $\nu_1 = 1$  conducts magnons, a distinct insulating state characterized by the total suppression of magnon transport obtains for  $0.89 \lesssim \nu_1 < 1$  on the hole side and  $1 < \nu_1 \lesssim 1.06$  on the electron side of  $\nu = 1$ . To within experimental error, arbitrarily small doping of the  $\nu_1 = 1$  state appears sufficient to fully suppress magnon transport. At high temperatures, where charge conductivity indicates the electron solid has melted, magnon transport is restored (Fig. 2f).

We propose that the suppression of magnon transport in the electron solid near  $\nu_1 = 1$  implies that charge solidification is accompanied by noncollinear spin textures—the low-doping insulating phase is a skyrmion solid, rather than a spin polarized electron solid. In the skyrmion solid phase, dilute charge carriers are localized by a combination of their mutual Coulomb repulsion and, potentially, disorder, while the electron spins are driven by exchange interactions into large-scale noncollinear ground state spin textures. Fig. 2g outlines a mechanism for the resulting suppression of magnon transport. Magnons are launched through the  $\nu_{II} = 1$  region, where they are gapped ( $E_M(k) \geq E_Z$ , with  $E_M(k)$  the magnon dispersion) and characterized by quantized spin. However, within the skyrmion solid phase, the excitation spectrum includes spin modes with  $E < E_Z$ [36]. When a magnon with energy  $E_Z$  enters the skyrmion solid phase, it can decay to one or more gapless spin modes (as well as one or more spinless phonons). Because a magnon with  $E < E_Z$  cannot enter the  $\nu = 1$  region surrounding the detector, the spins will be trapped in the skyrmion solid phase. The low energy magnons ultimately relax their energy and angular momentum outside the spin system, for example at the sample boundary, and generate no nonlocal voltage in the detector region.

Electron solids are also predicted to occur in the vicinity of FQH states[37], and evidence for such phases was recently reported in microwave spectroscopy experiments[38]. Figs. 3a and b show the low temperature behavior of  $G$  at  $B_\perp = 13.5$ T in the vicinity of  $\nu = 1/3$  and  $2/3$ . As is the case near integer  $\nu$ ,  $G$  undergoes a metal-insulator transition at  $T \approx 300$ mK, suggestive of new solid phases. Intriguingly, the strong non-local response at precise fractional filling is subtly suppressed upon doping (3c and d). Subtle features associated with an increased threshold for nonlocal response appear adjacent to the FQH states. This is reminiscent of the response of the skyrmion solids near  $\nu = 1$ , albeit with a dramatically lower threshold  $V_{\text{bias}}$  for the restoration of nonlocal response. Our data thus suggest that noncollinear spin-textured ground states

of fractional skyrmions may prevail near these fillings. We expect that additional experiments at lower temperatures and magnetic field (see Fig. S3) and in cleaner samples may reveal a plethora of additional spin textured phases, allowing the interacting phase diagram of two dimensional electrons to be mapped in great detail.

## METHODS

Devices were fabricated using a dry transfer procedure, following Refs. [9, 10]. An optical image of the device discussed in the main text is shown in Fig. M1. The monolayer graphene (MLG), graphite, and hexagonal-boron nitride (hBN) flakes were prepared by mechanical exfoliation. In the device described in the main text, the thicknesses of the hBN flakes above and below the MLG flake are 34 nm and 40 nm respectively. Top and bottom graphite gates were patterned as shown in Fig. 2a using plasma etching. The chosen shape of the gates yields three distinct MLG regions; the carrier density in each of them can be controlled independently. Region I (rendered in white in Fig. 1a) is exposed to and therefore controlled by the top and bottom graphite gates; region II (rendered in pink) is controlled by the top graphite gate and silicon gate; region III (rendered in green) is controlled by the silicon gate alone. In contrast to prior work, in our devices each internal ‘island,’ defined as a region completely surrounded by sample bulk at filling  $\nu_I$ , features two separate contacts which enable both calibration of the filling factors  $\nu_{II}$  and  $\nu_{III}$  as well as the injection and detection of magnons.

Transport measurements of the device were done in a dilution refrigerator equipped with a 14T superconducting magnet and heavy RF and audio frequency filtering with a cutoff frequency of  $\sim 10$  kHz. The measurements were performed at base temperature unless indicated, corresponding to a measured temperature of  $\lesssim 20$  mK on the probe. The temperature-dependent measurements were done by controlling the temperature using a heater mounted on a mixing chamber plate.

Fig. M2a shows a schematic measurement of the conductance  $G$ , proportional to the conductivity in region I. While the device design ensures edge state coupling between the contact and the boundary of region II, considerable care must be taken to ensure that the measured  $G$  is not dominated by spurious series resistances arising from the I/II interface. To address this source of systematic error, the filling factor of region II is tuned to a bulk conducting state using  $V_T$ . The value of  $V_T$  that maximizes the conductivity of region II is found from a two-dimensional sweep of  $V_T$  and  $V_B$  with silicon gate voltage  $V_{Si}$  fixed. In practice, we find that setting  $|\nu_I - \nu_{II}| < 1$  avoids high series resistances from an insulating I/II interface.  $\nu_I$  is then controlled using the bottom gate voltage  $V_B$ . Fig. M2b shows a typical trace of  $G$  as a function of  $V_B$  at  $B_\perp = 8$ T. The differential conductance was measured using a lock-in amplifier with a  $100 \mu\text{V}$  excitation at 17.777 Hz.

The measurements of the non-local response due to magnon transport require precise tuning of regions II and III to  $\nu_{II} = 1$

and  $\nu_{III} = 2$ . To find the required values of the gate voltages  $V_T^*$  and  $V_{Si}^*$  for a given  $B_{\perp}$  we first measure the intra-island conductance, as shown in Fig. M2c, as a function of  $V_{Si}$  with  $V_T$  and  $V_B$  set to zero. We choose a value of  $V_{Si}^*$  at which  $G = 2e^2/h$ , ensuring  $\nu_{III} \approx 2$ . Next, we measure intra-island conductance as a function of  $V_T$  at  $V_{Si} = V_{Si}^*$ ,  $V_B = 0$  and pick the value  $V_T^*$  at which  $G = e^2/h$  (Fig. M2d).  $V_T^*$  and  $V_{Si}^*$  are then fixed for the nonlocal measurements described in the main text. Nonlocal measurements are performed with  $V_{ex} \approx 0.075V_Z$  at 1234.5 Hz. The higher frequency significantly reduced the noise level while introducing negligible phase shift.

#### ACKNOWLEDGMENTS:

The authors acknowledge discussions with B. Halperin, C. Huang, A. Macdonald, and M. Zalatel. Experimental work at UCSB was supported by the Army Research Office under awards MURI W911NF-16-1-0361 and W911NF-16-1-0482. KW and TT acknowledge support from the Elemental Strategy Initiative conducted by the MEXT, Japan and and the CREST (JPMJCR15F3), JST. AFY acknowledges the support of the David and Lucile Packard Foundation and and Alfred. P. Sloan Foundation.

#### AUTHOR CONTRIBUTIONS:

HZ and HP fabricated the devices. HZ, HP and AFY performed the measurements and analyzed the data. HZ and AFY wrote the manuscript. TT and KW grew the hexagonal boron nitride crystals.

- 
- [1] Pui K. Lam and S. M. Girvin. Liquid-solid transition and the fractional quantum-Hall effect. *Physical Review B*, 30(1):473–475, July 1984.
- [2] D. Levesque, J. J. Weis, and A. H. MacDonald. Crystallization of the incompressible quantum-fluid state of a two-dimensional electron gas in a strong magnetic field. *Physical Review B*, 30(2):1056–1058, July 1984.
- [3] L. Brey, H. A. Fertig, R. Ct, and A. H. MacDonald. Skyrmie Crystal in a Two-Dimensional Electron Gas. *Physical Review Letters*, 75(13):2562–2565, September 1995.
- [4] S. L. Sondhi, A. Karlhede, S. A. Kivelson, and E. H. Rezayi. Skyrmions and the crossover from the integer to fractional quantum Hall effect at small Zeeman energies. *Phys. Rev. B*, 47(24), June 1993.
- [5] H. A. Fertig, L. Brey, R. Cote, and A. H. MacDonald. Charged spin-texture excitations and the Hartree-Fock approximation in the quantum Hall effect. *Phys. Rev. B*, 50(15), October 1994.
- [6] H. W. Jiang, R. L. Willett, H. L. Stormer, D. C. Tsui, L. N. Pfeiffer, and K. W. West. Quantum liquid versus electron solid around  $\nu = 1/5$  Landau-level filling. *Physical Review Letters*, 65(5):633–636, July 1990.
- [7] V. J. Goldman, M Santos, M Shayegan, and J. E. Cunningham. Evidence for two-dimensional quantum Wigner crystal. *Physical Review Letters*, 65(17):2189–2192, October 1990.
- [8] H. W. Jiang, H. L. Stormer, D. C. Tsui, L. N. Pfeiffer, and K. W. West. Magnetotransport studies of the insulating phase around  $\nu = 1/5$  Landau-level filling. *Physical Review B*, 44(15):8107–8114, October 1991.
- [9] H. Polshyn, H. Zhou, E.M. Spanton, T. Taniguchi, K. Watanabe, and A.F. Young. Quantitative Transport Measurements of Fractional Quantum Hall Energy Gaps in Edgeless Graphene Devices. *Physical Review Letters*, 121(22):226801, November 2018.
- [10] Y. Zeng, J. I. A. Li, S. A. Dietrich, O. M. Ghosh, K. Watanabe, T. Taniguchi, J. Hone, and C. R. Dean. High quality magnetotransport in graphene using the edge-free Corbino geometry. *arXiv:1805.04904 [cond-mat]*, May 2018. *arXiv: 1805.04904*.
- [11] Di S. Wei, Toeno van der Sar, Seung Hwan Lee, Kenji Watanabe, Takashi Taniguchi, Bertrand I. Halperin, and Amir Yacoby. Electrical generation and detection of spin waves in a quantum Hall ferromagnet. *Science*, 362(6411):229–233, October 2018.
- [12] Petr Stepanov, Shi Che, Dmitry Shcherbakov, Jiawei Yang, Ruoyu Chen, Kevin Thilagar, Greyson Voigt, Marc W. Bockrath, Dmitry Smirnov, Kenji Watanabe, Takashi Taniguchi, Roger K. Lake, Yafis Barlas, Allan H. MacDonald, and Chun Ning Lau. Long-distance spin transport through a graphene quantum Hall antiferromagnet. *Nature Physics*, page 1, June 2018.
- [13] S. M. Girvin. The Quantum Hall Effect: Novel Excitations And Broken Symmetries. In A. Comtet, T. Jolicur, S. Ouvry, and F. David, editors, *Aspects topologiques de la physique en basse dimension. Topological aspects of low dimensional systems*, Les Houches - Ecole d’Ete de Physique Theorique, pages 53–175. Springer Berlin Heidelberg, 1999.
- [14] V. Bayot, E. Grivei, S. Melinte, M. B. Santos, and M. Shayegan. Giant Low Temperature Heat Capacity of GaAs Quantum Wells near Landau Level Filling  $\nu = 1$ . *Physical Review Letters*, 76(24):4584–4587, June 1996.
- [15] V. Bayot, E. Grivei, J.-M. Beuken, S. Melinte, and M. Shayegan. Critical Behavior of Nuclear-Spin Diffusion in GaAs/AlGaAs Heterostructures near Landau Level Filling  $\nu = 1$ . *Physical Review Letters*, 79(9):1718–1721, September 1997.
- [16] S. Melinte, E. Grivei, V. Bayot, and M. Shayegan. Heat Capacity Evidence for the Suppression of Skyrmions at Large Zeeman Energy. *Physical Review Letters*, 82(13):2764–2767, March 1999.
- [17] Han Zhu, G. Sambandamurthy, Yong P. Chen, P. Jiang, L. W. Engel, D. C. Tsui, L. N. Pfeiffer, and K. W. West. Pinning-Mode Resonance of a Skyrmie Crystal near Landau-Level Filling Factor  $\nu = 1$ . *Physical Review Letters*, 104(22):226801, June 2010.
- [18] S. E. Barrett, G. Dabbagh, L. N. Pfeiffer, K. W. West, and R. Tycko. Optically Pumped NMR Evidence for Finite-Size Skyrmions in GaAs Quantum Wells near Landau Level Filling  $\nu = 1$ . *Phys. Rev. Lett.*, 74(25):5112, June 1995.
- [19] E. H. Aifer, B. B. Goldberg, and D. A. Broido. Evidence of Skyrmion Excitations about  $\nu = 1$  in n-Modulation-Doped Single Quantum Wells by Interband Optical Transmission. *Physical Review Letters*, 76(4):680–683, January 1996.
- [20] J. H. Smet, R. A. Deutschmann, F. Ertl, W. Wegscheider, G. Abstreiter, and K. von Klitzing. Gate-voltage control of spin interactions between electrons and nuclei in a semiconductor. *Nature*, 415(6869):281–286, January 2002.

- [21] W. Desrat, D. K. Maude, M. Potemski, J. C. Portal, Z. R. Wasilewski, and G. Hill. Resistively Detected Nuclear Magnetic Resonance in the Quantum Hall Regime: Possible Evidence for a Skyrme Crystal. *Physical Review Letters*, 88(25):256807, June 2002.
- [22] G. Gervais, H. L. Stormer, D. C. Tsui, P. L. Kuhns, W. G. Moulton, A. P. Reyes, L. N. Pfeiffer, K. W. Baldwin, and K. W. West. Evidence for Skyrmion Crystallization from NMR Relaxation Experiments. *Physical Review Letters*, 94(19):196803, May 2005.
- [23] L. A. Tracy, J. P. Eisenstein, L. N. Pfeiffer, and K. W. West. Resistively detected NMR in a two-dimensional electron system near  $\nu=1$ : Clues to the origin of the dispersive lineshape. *Physical Review B*, 73(12):121306, March 2006.
- [24] V. F. Mitrovi, M. Horvati, C. Berthier, S. A. Lyon, and M. Shayegan. NMR study of large skyrmions in  $\text{AlO}_2/\text{GaAs}$  quantum wells. *Physical Review B*, 76(11):115335, September 2007.
- [25] L. Tiemann, T. D. Rhone, N. Shibata, and K. Muraki. NMR profiling of quantum electron solids in high magnetic fields. *Nature Physics*, 10(9):648–652, September 2014.
- [26] B.A. Piot, W. Desrat, D.K. Maude, D. Kazazis, A. Cavanna, and U. Gennser. Disorder-Induced Stabilization of the Quantum Hall Ferromagnet. *Physical Review Letters*, 116(10):106801, March 2016.
- [27] C. R. Dean, A. F. Young, P. Cadden-Zimansky, L. Wang, H. Ren, K. Watanabe, T. Taniguchi, P. Kim, J. Hone, and K. L. Shepard. Multicomponent fractional quantum Hall effect in graphene. *Nature Physics*, 7(9):693–696, 2011.
- [28] A. F. Young, C. R. Dean, L. Wang, H. Ren, P. Cadden-Zimansky, K. Watanabe, T. Taniguchi, J. Hone, K. L. Shepard, and P. Kim. Spin and valley quantum Hall ferromagnetism in graphene. *Nature Physics*, 8(7):550–556, July 2012.
- [29] Benjamin E. Feldman, Benjamin Krauss, Jurgen H. Smet, and Amir Yacoby. Unconventional Sequence of Fractional Quantum Hall States in Suspended Graphene. *Science*, 337(6099):1196–1199, October 2012.
- [30] Shaowen Chen, Rebeca Ribeiro-Palau, Kang Yang, Kenji Watanabe, Takashi Taniguchi, James Hone, Mark O. Goerbig, and Cory R. Dean. Competing Fractional Quantum Hall and Electron Solid Phases in Graphene. *Physical Review Letters*, 122(2):026802, January 2019.
- [31] Yang Liu, C. G. Pappas, M. Shayegan, L. N. Pfeiffer, K. W. West, and K. W. Baldwin. Observation of Reentrant Integer Quantum Hall States in the Lowest Landau Level. *Physical Review Letters*, 109(3):036801, July 2012.
- [32] R. Ct and A. H. MacDonald. Spin-ordering and magnon collective modes for two-dimensional electron lattices in strong magnetic fields. *Physical Review B*, 53(15):10019–10029, April 1996.
- [33] Maxim Kharitonov. Phase diagram for the  $\nu=0$  quantum Hall state in monolayer graphene. *Phys. Rev. B*, 85(15):155439, April 2012.
- [34] C. Kallin and B. I. Halperin. Excitations from a filled Landau level in the two-dimensional electron gas. *Physical Review B*, 30(10):5655–5668, November 1984.
- [35] A. H. MacDonald and J. J. Palacios. Magnons and Skyrmions in fractional Hall ferromagnets. *Physical Review B*, 58(16):R10171–R10174, October 1998.
- [36] R. Cote, A. H. MacDonald, Luis Brey, H. A. Fertig, S. M. Girvin, and H. T. C. Stoof. Collective Excitations, NMR, and Phase Transitions in Skyrme Crystals. *Physical Review Letters*, 78(25):4825–4828, June 1997.
- [37] Alexander C. Archer and Jainendra K. Jain. Static and dynamic properties of type-II composite fermion Wigner crystals. *Physical Review B*, 84(11):115139, 2011.
- [38] Han Zhu, Yong P. Chen, P. Jiang, L. W. Engel, D. C. Tsui, L. N. Pfeiffer, and K. W. West. Observation of a pinning mode in a Wigner solid with  $\nu = 1/3$  fractional quantum Hall excitations. *Physical Review Letters*, 105(12):126803, 2010.
- [39] A. A. Zibrov, E. M. Spanton, H. Zhou, C. Kometter, T. Taniguchi, K. Watanabe, and A. F. Young. Even-denominator fractional quantum Hall states at an isospin transition in monolayer graphene. *Nature Physics*, 14(9):930–935, September 2018.
- [40] F. Amet, J. R. Williams, K. Watanabe, T. Taniguchi, and D. Goldhaber-Gordon. Insulating Behavior at the Neutrality Point in Single-Layer Graphene. *Physical Review Letters*, 110(21):216601, May 2013.
- [41] B. Hunt, J. D. Sanchez-Yamagishi, A. F. Young, M. Yankowitz, B. J. LeRoy, K. Watanabe, T. Taniguchi, P. Moon, M. Koshino, P. Jarillo-Herrero, and R. C. Ashoori. Massive Dirac Fermions and Hofstadter Butterfly in a van der Waals Heterostructure. *Science*, 340:1427–1430, 2013.

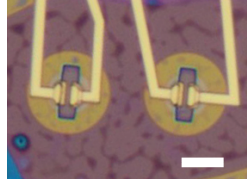


FIG. M1. **Optical micrograph of the device.** Scale bar corresponds to  $5 \mu\text{m}$ .

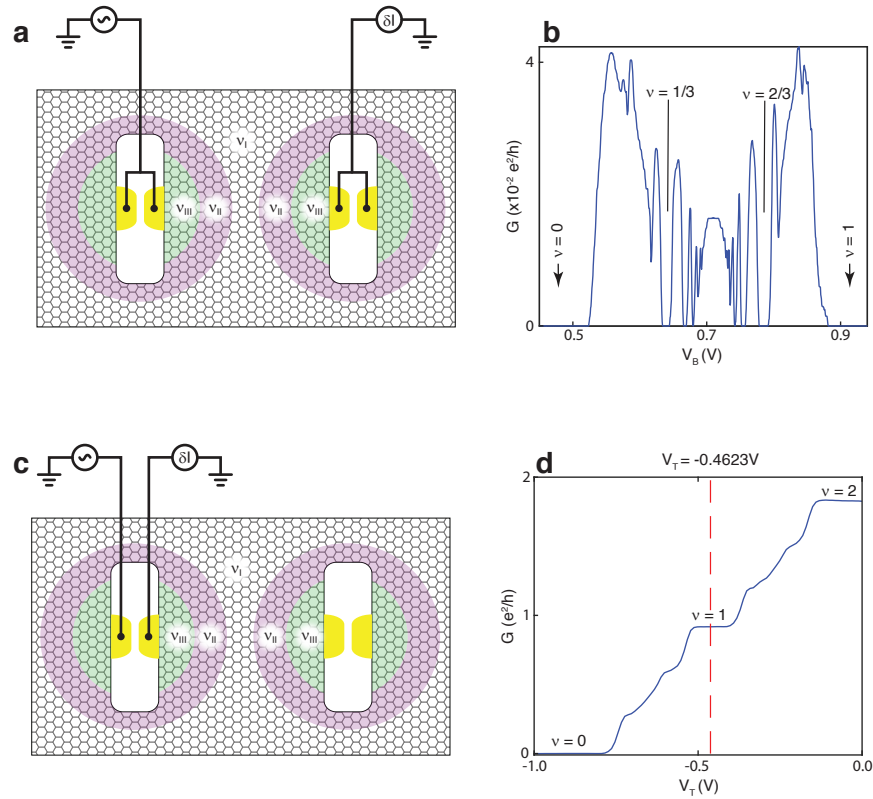


FIG. M2. **Methods of local transport measurements.** **a**, Inter-island transport measurement, referred to as  $G$  in the main text. Because there is no edge state that directly couples charge across the pink region, non-zero  $G$  is measured only when  $\nu_{II}$  is tuned to a bulk conducting filling factor. Moreover,  $|\nu_{II} - \nu_I|$  should be less than 1 to avoid fringe field-induced insulating phase between the pink and white region. **b**, Inter-island transport trace at  $B_{\perp} = 8\text{T}$  between  $\nu = 0$  to  $\nu = 1$ . **c**, Intra-island transport. The two contacts on the right-hand side are kept open, and the two terminal resistance within a single island is measured. **d**, Typical intra-island transport trace at  $B_{\perp} = 8\text{T}$ . The silicon gate voltage is fixed at  $10\text{V}$ . The result shows that by fixing the silicon gate at  $10\text{V}$  and the top gate at  $-0.4623\text{V}$ , we can set  $\nu_{III} \geq 2$  and  $\nu_{II} = 1$ .

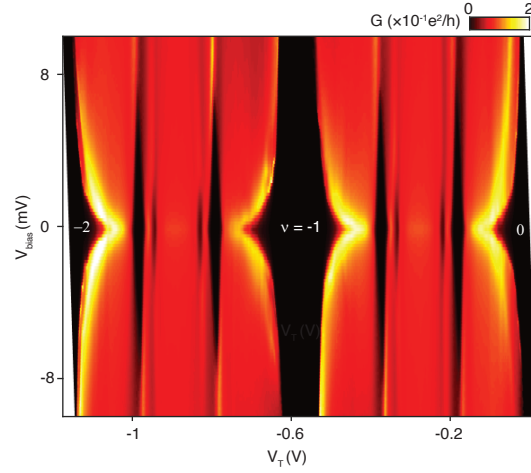


FIG. S1. **Non-linear transport near  $\nu = -1$ .** Differential conductance  $G$  as a function of gate voltage  $V_T$  and source-drain bias voltage  $V_{\text{bias}}$  measured in a second device at  $B_{\perp} = 8\text{T}$ . Strong nonlinearity is observed near all integer fillings.

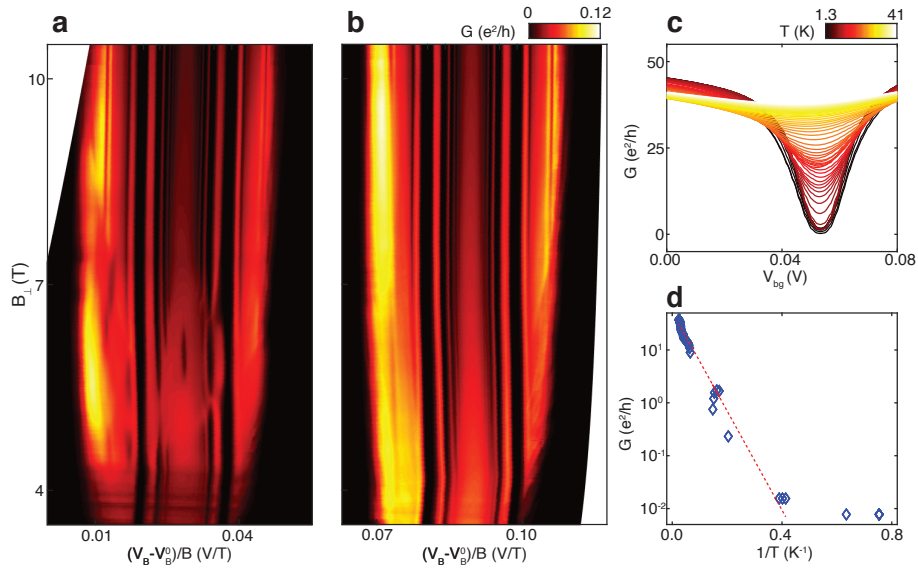
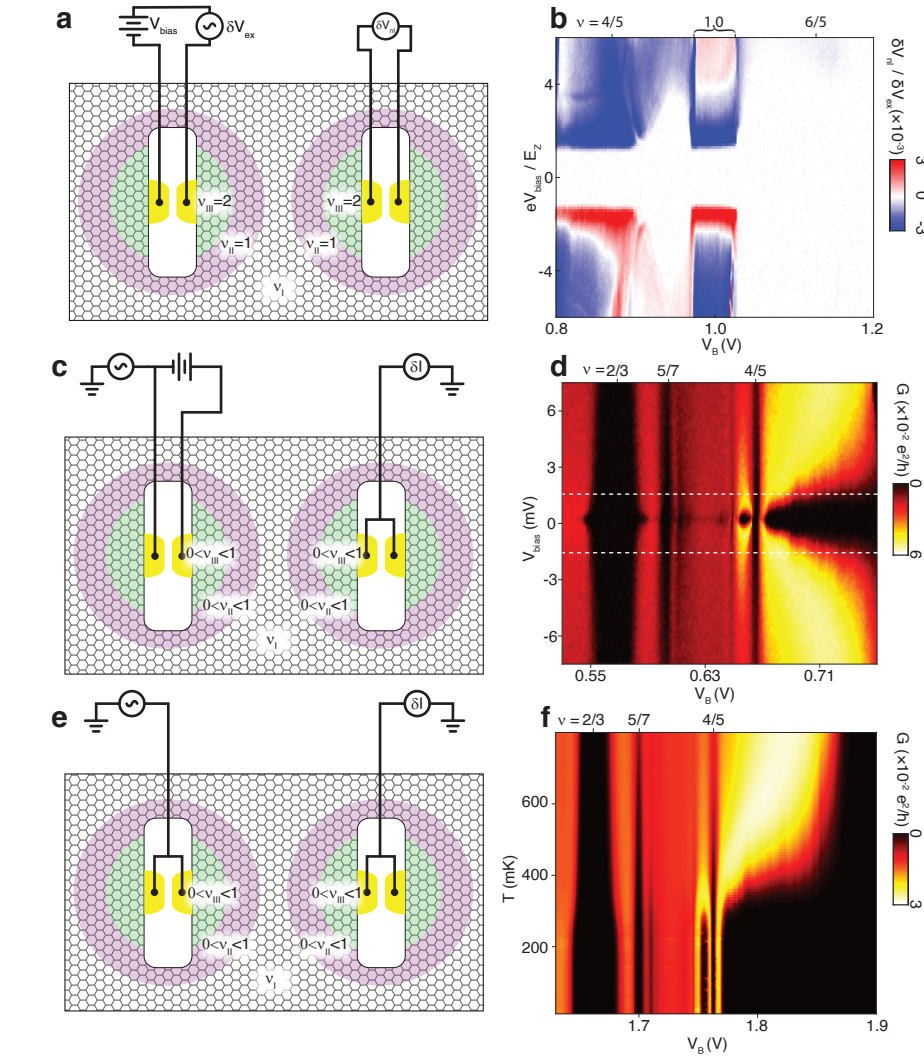


FIG. S2. **Transport characterization of the device.** **a** Conductance as function of carrier density and magnetic field for  $0 < \nu < 1$  and **b** for  $0 < \nu < 2$ . The device shows a series of FQH phase transitions for  $0 < \nu < 1$ , including the appearance of an even denominator state at  $\nu = 1/2$  over a narrow range of magnetic fields, all of which are absent for  $1 < \nu < 2$ [39]. **c**, Conductance near the charge neutrality point at  $B = 0$  at different temperatures. **d**, Arrhenius plot of the conductance at the charge neutrality point, showing simply activated behavior consistent with a substrate induced sublattice splitting[40, 41]. The thermal activation gap is measured to be 3.7 meV.





**FIG. S3. Joule heating and its effect on the nonlocal measurement.** **a**, Schematic for measurements of the nonlocal response. A DC bias is applied between the two left contacts, which are tuned to have an intra-island conductance  $G = e^2/h$ . This results in a power dissipated via Joule heating of  $P = V_{\text{bias}}^2 G$ . At the Zeeman threshold,  $V_{\text{bias}} = E_Z/e$ , resulting in  $P = E_Z^2/h \approx .52\text{pW} \times B_{\text{[Tesla]}}^2$ . **b**, As described in the main text, strong magnon transport signals are observed only for  $V_{\text{bias}} > E_Z/e$ , where the Joule heating power, dissipated directly on the device, leads to nonnegligible heating of the electron system. Data shown here are measured at  $B=10\text{T}$ . **c**, Experimental setup for determining the effects of Joule heating. In this setup, a bias voltage is applied across one island, as in the nonlocal measurement, but region II is tuned to be conducting. This allows current to flow to the other island and the local conductivity to be measured as a function of both  $V_B$  and the bias voltages. Note that the small local conductance across region I,  $G \approx .01e^2/h$ , ensures that only minimal power is evolved from DC current flow across the sample bulk, providing a good proxy for heating in the nonlocal configuration. **d**, Local conductivity measured in the setup described in panel c as a function of  $V_{\text{bias}}$  and  $V_B$  at  $B=13.5\text{T}$ . As is evident in the data, applied bias leads to rapid degradation of the insulating phases associated with electron solids near  $\nu_I = 2/3, 4/5$ , and 1. At the  $V_{\text{bias}} = \pm E_Z/e$  (indicated by dashed white lines), only a portion of the electron solid proximal to  $\nu = 1$  still shows insulating behavior. **e**, Experimental setup for local conductance measurement. **f**, Local conductance as a function of temperature at  $B=13.5\text{T}$ . Comparing with the bias dependence shown in panel d, we conclude that bias-induced heating bring the electron temperature to  $T \approx 400\text{mK}$  at  $eV_{\text{bias}} \approx E_Z$ . Notably, because the Zeeman energy sets the minimal bias voltage required to launch magnons, the effects of Joule heating grow significantly worse at high fields, scaling as  $B^2$ . In contrast, the Coulomb interaction scales as  $e^2/l_b \propto B_{\perp}^{1/2}$ . The competition between the Coulomb interaction and sample heating limits the range of  $B_{\perp}$  in which the electron solid phase exists when  $eV_{\text{bias}} > E_Z$ . Specifically, at large  $B_{\perp}$ , the electron solid melts when  $eV_{\text{bias}} > E_Z$  due to heating. We believe bias-induced Joule heating is primarily responsible for our observation of possible fractional skyrmion solids only at  $B_{\perp} = 7\text{T}$ , but not at larger  $B_{\perp}$  where they are more developed. Interestingly, the low-B limit in our experiment is set not by the absence of correlation physics in region I, but rather by the breakdown of quantum Hall ferromagnetism in the much more disordered region II, which is exposed through the hBN dielectric to a disordered hBN/SiO<sub>2</sub> interface. It may thus be possible to significantly improve on the current measurements by constructing devices in which all three necessary regions are of comparable sample quality.

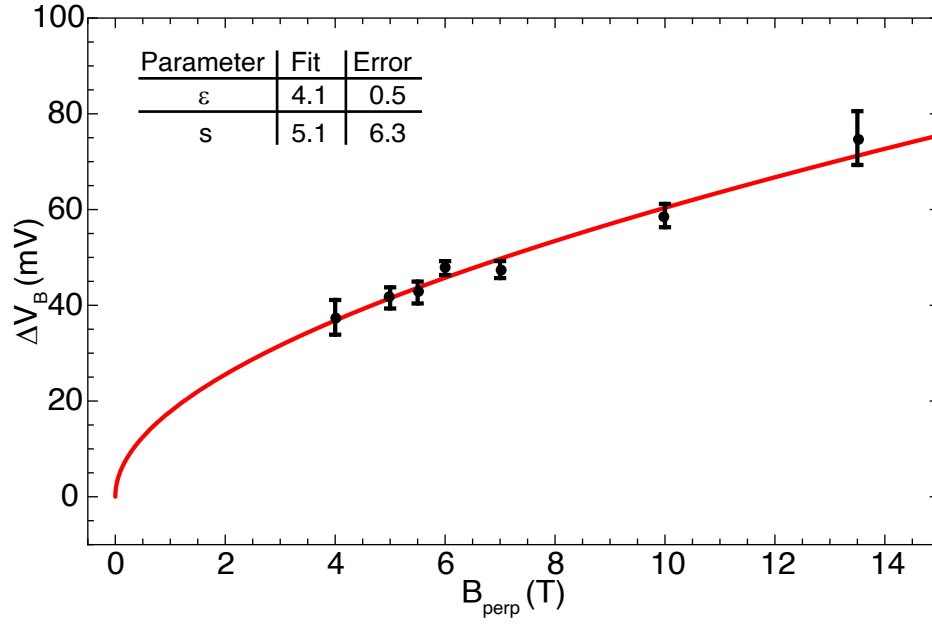


FIG. S4. **Comparison of measured  $\nu_1 = 1$  gap to theoretical calculation.** Symbols indicate the measured width,  $\Delta V_B$ , corresponding to large nonlocal response, plotted for a variety of magnetic fields. Theoretically,  $\Delta V_B$  should directly give the energy gap of the quantum Hall ferromagnet ( $\Delta$ ) via the relation  $e\Delta V_B = \Delta$ .  $\Delta$  itself is predicted to follow the relation  $\Delta = \sqrt{\frac{\pi}{2} \frac{e^2}{\epsilon \ell_B}} + sg\mu_B B_T$  (here  $\epsilon$  is the dielectric constant and  $s = 2K + 1$  tracks the number of excess spin flips,  $K$ , within a skyrmion excitation). The red curve represents a best fit to the measured data with  $\epsilon$  and  $s$  as free parameters. Due to the small contribution of the Zeeman energy to the total gap,  $s$  is not well constrained, with a best fit of  $5.1 \pm 6$ . This fit is thus unable to discriminate between small skyrmions and single spin flip excitations, but is consistent with theoretical predictions of small skyrmions in the experimental range of  $E_Z/E_C$ . The best fit parameter  $\epsilon = 4.1 \pm .5$  agrees, to within error, with the expected value of  $\epsilon = \sqrt{3 \times 6.6} \approx 4.4$ , consisting of the geometric average of the in- and out-of-plane dielectric constants of the encapsulating hBN layers. Note that Landau level broadening was recently measured to be  $< 1$  meV in similar devices[9, 10], and is thus negligible on the scale of the  $\nu = 1$  energy gap over the measured range of magnetic fields.